Supersonic flows of dense gases in cascade configurations

By J. F. MONACO[1], M. S. CRAMER[1] and L. T. WATSON[2]

[1] Department of Engineering Science and Mechanics, Virginia Polytechnic Institute and State University, Blacksburg, VA 24061, USA

[2] Department of Computer Science, Virginia Polytechnic Institute and State University, Blacksburg, VA 24061, USA

We examine the steady, inviscid, supersonic flow of Bethe–Zel'dovich–Thompson (BZT) fluids in two-dimensional cascade configurations. Bethe–Zel'dovich–Thompson fluids are single-phase gases having specific heats so large that the fundamental derivative of gasdynamics, Γ, is negative over a finite range of pressures and temperatures. The equation of state is the well-known Martin–Hou equation, and the numerical scheme is the explicit predictor–corrector method of MacCormack. Numerical comparisons between BZT fluids and lighter fluids such as steam are presented. It was found that the natural dynamics of BZT fluids can result in significant reductions in the adverse pressure gradients associated with the collision of compression waves with neighbouring turbine blades. A numerical example of an entirely isentropic supersonic cascade flow is also presented.

1. Introduction

One of the major loss mechanics in transonic and supersonic turbomachinery is that due to the generation of shock waves. In addition to the irreversibility of the shock waves themselves, the collision of shock waves with neighbouring blades can cause both boundary layer transition and separation. The largest losses are due to separation which can also cause significant vibration and noise. The purpose of the present investigation is to provide evidence for the idea that such losses are not inevitable, particularly when fluids other than low-pressure air and steam are considered. It is of particular interest to note that the possible advantages described here are due to the natural dynamics of the fluids considered and not due to extensive redesign of the turbine blades and other hardware.

One of the most common methods for the study of compressible flows is through the use of the ideal gas model. This approximation works reasonably well for fluids operating at low pressures, and it is an attractive model to use because it often results in the recovery of an exact, closed-form solution. Furthermore, the ideal gas model is particularly easy to incorporate in modern numerical schemes. However, in high-pressure applications, the ideal gas theory may no longer give an accurate representation of the fluid response. In order to obtain results that describe the qualitative as well as the quantitative behaviour observed in practice, it becomes necessary to consider more complex equations of state that more accurately model the response of the fluid.

Heat transfer and turbomachinery equipment in both subcritical and supercritical Rankine power cycles frequently involve dense gas effects; see, e.g. Jones & Hawkins

(1972) or Reynolds & Perkins (1977). Other applications in which such high-pressure effects are important include the hypersonic and transonic wind tunnel designs described by Enkenhus & Parazzoli (1970), Wagner & Schmidt (1978), Simeonides (1987, 1990), Anderson (1991 *a*, *b*), and Anders (1993). Applications involving dense gas effects in chemical and fuel transport are discussed by Leung & Epstein (1988) and Bober & Chow (1990). A third class of dense gas work is that using supercritical H_2 to cool hypersonic aircraft and is described in the article by Dziedzic *et al.* (1993).

Distinct qualitative differences occur between the dense gas theory and the ideal gas approximation under certain conditions. Thompson (1971) was the first to point out the importance of the fundamental derivative

$$\Gamma = \Gamma(\rho, s) \equiv \frac{a}{\rho} + \frac{\partial a}{\partial \rho}\bigg|_s \qquad (1.1)$$

to virtually all aspects of gasdynamics. Here $a = (\partial p / \partial \rho)^{1/2}|_s$ is the thermodynamic sound speed, and ρ, s, p are the fluid density, entropy and pressure. In general, non-classical results are observed when Γ becomes negative over a finite range of temperatures and pressures in the flow, although some effects require only that $\rho\Gamma/a$ be less than unity. The conditions under which $\Gamma < 0$ have been discussed in detail by Bethe (1942), Zel'dovich (1946), Lambrakis & Thompson (1972), and Thompson & Lambrakis (1973), and as a result, the fluids which have $\Gamma < 0$ over a finite range of pressures and temperatures in the single-phase regime are referred to as Bethe–Zel'dovich–Thompson (BZT) fluids after the authors who first recognized the importance of (1.1).

For reference, we note that the expression for the fundamental derivative of a perfect gas, i.e. an ideal gas having constant specific heats, is given by

$$\tilde{\Gamma} = \tfrac{1}{2}(\gamma + 1), \qquad (1.2)$$

where γ is the ratio of specific heats and $\tilde{\Gamma}$ is the non-dimensional version of the fundamental derivative, i.e.

$$\tilde{\Gamma} = \rho\Gamma/a. \qquad (1.3)$$

The usual inequalities that guarantee the stability of the thermodynamic equilibrium of any fluid imply that γ is strictly greater than unity. Thus, in the perfect gas limit, $\tilde{\Gamma}$ is necessarily bounded from below by unity, and as a result, the non-classical behaviours that are associated with a negative fundamental derivative are not observed when a perfect gas model is being used.

Bethe (1942) and Zel'dovich (1946) pointed out that the expression for Γ of dense gases is considerably more complicated than that found in the perfect gas theory, and that the values of Γ may be less than unity, even becoming negative in fluids with sufficiently large specific heats. For such a fluid, the region in which $\Gamma < 0$ is in the neighbourhood of the saturation curve at pressures on the general order of those of the thermodynamic critical point. As an illustration, we have plotted various constant Γ contours for a van der Waals gas with constant specific heat $c_{v\infty} = 50R$ in figure 1. Here $c_{v\infty}$ is the zero-pressure specific heat at constant volume and R is the usual gas constant.

In order to give examples of negative-Γ fluids as well as to illustrate the general variation of Γ, we have plotted the variation of $\rho\Gamma/a$ with normalized density, ρ/ρ_c, evaluated along the critical isotherm in figure 2. Here the subscript c refers to the value of the property of interest evaluated at the thermodynamic critical point. The fluids chosen are molecular nitrogen (N_2), steam (H_2O), octane (C_8H_{18}), and four
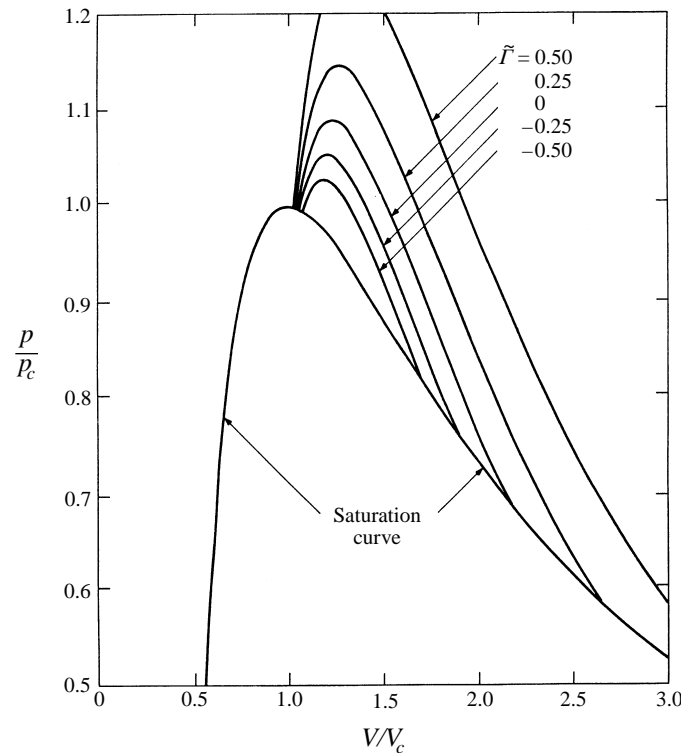
FIGURE 1. Constant $\tilde{\Gamma} \equiv \rho \Gamma / a$ contours. The fluid is a van der Waals gas with $c_{v\infty} = 50R$.

commercially available heat transfer fluids: FC-72 (C_6F_{14}), PP9 ($C_{11}F_{20}$), PP11 ($C_{14}F_{24}$), and FC-71 ($C_{18}F_{39}N$). The physical properties of the first three fluids were taken from Reid, Prausnitz & Poling (1987) and those of FC-72 and PP9 were obtained from the manufacturers' technical publications. The physical properties of PP11 and FC-71 were estimated by Cramer (1989a). The equation of state that is used to generate figure 2 is that due to Martin & Hou (1955) which is discussed briefly in §5. In figure 2, the main point of interest is that the heavier fluids have a local minimum in $\tilde{\Gamma}$ at densities approximately equal to one-half to two-thirds the critical density. The heaviest fluids, namely PP11 and FC-71, have a finite region of $\Gamma < 0$ along the critical isotherm. Further examples of negative-Γ fluids are given in the articles by Thompson & Lambrakis (1973) and Cramer (1989a).

Recent reviews of the non-classical dynamics of BZT fluids have been given by Thompson (1971), Thompson & Lambrakis (1973), Menikoff & Plohr (1989), Leidner (1990), Cramer (1991a), and Kluwick (1991). The most cursory reading of any one of these reviews reveals the scientific motivation for the study of BZT fluids. Most of the practical interest in these fluids is due to the potential advantages of their use as working fluids in Rankine power cycles. Previous investigators have identified two physical effects which can lead to improved efficiency of such turbomachinery. The first is the narrowing of the range of Mach numbers corresponding to transonic flow. Remarkable increases in the lower critical Mach number have been reported by Morren (1991), Cramer, Tarkenton & Tarkenton (1992), Cramer & Tarkenton (1992), and Tarkenton & Cramer (1993). In a study of ordinary hydrocarbons, Cramer (1991b) has shown that the onset of transonic flow, as measured by the occurrence of
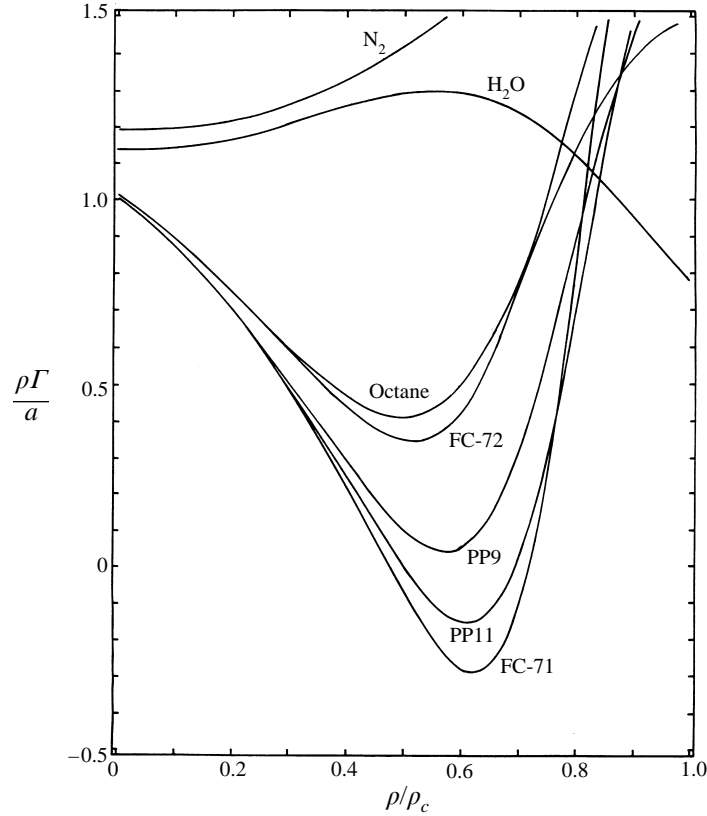
FIGURE 2. Variation of $\rho\Gamma/a$ along the critical isotherm of each fluid. The gas model in each case is that due to Martin & Hou (1955) with a power-law specific heat.

detachment, is delayed when heavy, dense gases are considered. We refer the reader to these publications for a summary of the relevant dynamics.

The second advantageous effect, and that of the most interest in the present study, is due to the fact that the well-known compression shocks of the perfect gas theory disintegrate whenever $\Gamma < 0$ at every point in the flow. The first to discuss such disintegrations in the context of steady flows was Thompson (1971) who pointed out that the classical oblique compression shock must be replaced by a centred compression fan for the flow of a negative-Γ fluid over a compression corner. In addition, Thompson also pointed out that the structure of any centred fan could be computed from

$$\frac{\mathrm{d}\psi}{\mathrm{d}\theta} = \frac{\rho\Gamma}{a}\frac{M^2}{M^2-1}, \qquad (1.4)$$

combined with the appropriate form of the Bernoulli equation and the equation of state. The quantities ψ, θ, and M are the Mach angle, flow deflection angle, and the local Mach number. Both the Mach angle and flow deflection angle are normally measured from the undisturbed flow direction. If we restrict our attention to a compression corner, i.e. $\mathrm{d}\theta > 0$, then it is clear that the Mach angle increases ($\mathrm{d}\psi > 0$) and therefore results in shock formation if $\Gamma > 0$ and that ψ decreases to form a centred fan if $\Gamma < 0$. To illustrate the difference between the ideal and dense gas theories, we have sketched the wave patterns when $\Gamma > 0$ and $\Gamma < 0$ fluids flow over
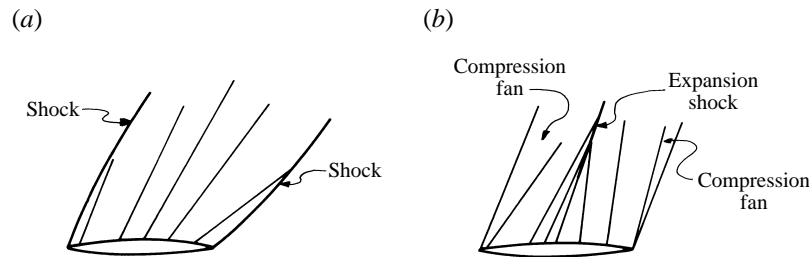
(*a*)   (*b*)

FIGURE 3. Sketch of the flow of (*a*) $\Gamma > 0$ fluid and (*b*) $\Gamma < 0$ fluid past a single airfoil.

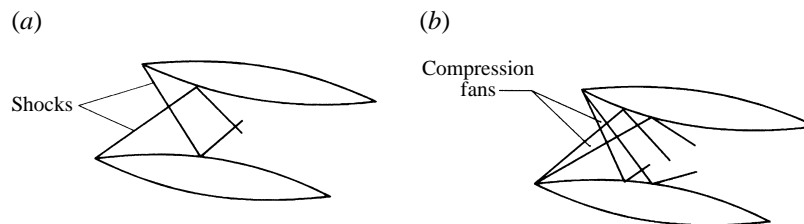(*a*)   (*b*)

FIGURE 4. Sketch of the flow of (*a*) $\Gamma > 0$ and (*b*) $\Gamma < 0$ fluid in a cascade configuration.

single airfoils in figure 3. In the $\Gamma < 0$ case, (1.4) can be used to show that the Mach lines originating in the expansive regions of the flow ultimately focus to form an expansion shock.

In order to see the advantages of BZT fluids we consider the cascade configurations sketched in figure 4. In each case the compression wave emanating from the leading edge of the lower blade is assumed to strike the lower side of the upper blade. Figure 4(*a*) corresponds to a $\Gamma > 0$ fluid, e.g. steam. In this case the compression is necessarily a shock wave. Because of the large adverse pressure gradient generated by the instantaneous pressure rise predicted by the inviscid theory, the boundary layer is likely to separate if the compression is sufficiently strong. In the case of the $\Gamma < 0$ fluid, the disintegration of the shock spreads the compression over a finite distance and therefore lowers the strength of the adverse pressure gradient for a pressure rise identical to that of the $\Gamma > 0$ case. As a result, it is expected that the possibility of shock-induced separation can be reduced when $\Gamma > 0$ fluids are replaced by $\Gamma < 0$ fluids.

A second advantage of BZT fluids is seen when we recall that the expansion shock generated by a smooth expansion requires a finite distance to form; one such formation is sketched in figure 3(*b*). If the formation distance is sufficiently large compared to the distance between the blades, the shock may not form in the vicinity of the blades. Thus, losses due to shock irreversibility appear to be completely eliminated. Furthermore, if the decrease in the adverse pressure gradient due to the disintegration of the compression shock results in an attached boundary layer, it appears that the flow in the cascade remains entirely isentropic, i.e. loss-free. A sketch of such an isentropic cascade is provided in figure 4(*b*).

Arguments for the existence of entirely isentropic supersonic cascades were originally given by Cramer (1991*a*) and were based on an extrapolation of the single-airfoil theory. Important complications not considered by Cramer include those due to the interaction between the Mach waves from the upper surface of the lower blade and the waves from the lower surface of the upper blade. One of the main contributions of the present investigation is to demonstrate that both advantages mentioned above can be realized in spite of such interactions.
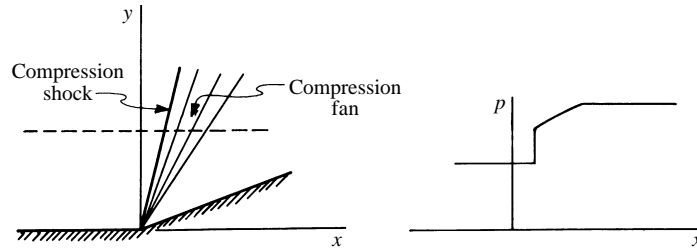
FIGURE 5. Sketch of a shock–fan and the corresponding pressure distribution
at the fixed height denoted by the dashed line.

A second set of complications is due to the fact that the region where $\Gamma < 0$ is of finite extent. Thus, the flow disturbances caused by the turbine blades can result in local regions of positive Γ, even if the undisturbed state corresponds to $\Gamma < 0$. When Γ changes sign within the centred compression fan sketched in figures 3 and 4, it can be shown that a compression shock necessarily appears either at the upstream side or the downstream side of the fan. Under some conditions, compression shocks can appear both upstream and downstream of the compression fan; this shock–fan–shock configuration is referred to as shock-splitting both here and in the unsteady, one-dimensional theory presented by Cramer (1989b, 1991a). The formation of triple-valued solutions and the resultant necessity of shock waves can be deduced from Thompson's result (1.4) which requires that the Mach angle ψ has an extremum at points where the fundamental derivative changes sign. The significance of the occurrence of shock waves is that the smooth isentropic compressions depicted in figures 3 and 4 are only possible for sufficiently weak compressions.

A second way to view shock–fan combinations is that they are the result of the partial disintegration of compression discontinuities. This is a particularly useful viewpoint when considering a flow with a free-stream state corresponding to $\Gamma > 0$. If the compression discontinuity is sufficiently strong it may be possible to compress the flow from the $\Gamma > 0$ region to one having $\Gamma < 0$. Under these conditions, the shock may remain intact or may undergo a partial disintegration into a shock followed by a compression fan. An example of such a partial disintegration is sketched in figure 5. Because only part of the compression is accomplished through a discontinuity and the strength of the shock remains unchanged with further increases in the strength of the overall compression, the partial disintegration process provides a limitation on the strength of compression shocks occurring in BZT fluids. Thus, it is expected that the probability of shock-induced separation will be reduced in spite of the occurrence of shock waves.

Limitations on the strength of compression shocks have been noted in the transonic flows discussed by Morren (1991), Cramer & Tarkenton (1992), Tarkenton & Cramer (1993), and Schnerr & Leidner (1993). The latter is closely related to the present investigation because of its use of cascade configurations. Detailed discussions of the partial disintegration of shock waves in steady supersonic flows of BZT fluids are found in the article by Cramer (1991a) and the thesis by Crickenberger (1991). The discussion in both of the latter references is limited to simple waves over single airfoil sections and therefore may be regarded as introductions to the present study.

In the present investigation we examine whether the advantages mentioned above can be realized in spite of the complications associated with wave interactions and the finite size of the region of negative Γ. The main focus is to illustrate the relevant physics

and we therefore restrict our attention to the simple case of two-dimensional, steady, inviscid flows of dense gases. The flow is taken to be entirely supersonic and therefore complements the transonic flow studies of Schnerr & Leidner (1993).

Because our main interest is in the compression waves striking neighbouring blades, the configuration chosen is a channel-like model. The principal difference between this model and an infinite periodic cascade is that the boundary downstream of each blade is rigid rather than one satisfying symmetry conditions. Although such a condition is reasonable for non-staggered, non-lifting blades, in more complex configurations our model fails to correctly capture the details of the wave system far behind the blades. However, because the flow is fully supersonic, the flow details between the blades remains unaffected by the simpler boundary condition.

The formulation of the Euler equations is found in §2. The gas model is the highly accurate Martin–Hou (1955) equation of state and is discussed in §5. Because we will restrict our attention to supersonic flows, the numerical scheme chosen is the well-known explicit predictor–corrector scheme of MacCormack (1969). Details of its implementation are found in §4. We discuss comparisons of our calculated results with known solutions in §6. In §7 we confine our attention to simple wedge flows in order to illustrate the various types of shock disintegration. Finally, in §8, we present our results for both lifting and non-lifting cascade configurations.

2. Formulation

The flow being considered here is assumed to be two-dimensional, inviscid, steady, single phase, and free of body forces. Under these conditions, the governing system of equations may be written as

$$\frac{\partial(\rho u)}{\partial x} + \frac{\partial(\rho v)}{\partial y} = 0, \tag{2.1}$$

$$\frac{\partial}{\partial x}(\rho u^2 + p) + \frac{\partial}{\partial y}(\rho uv) = 0, \tag{2.2}$$

$$\frac{\partial}{\partial x}(\rho uv) + \frac{\partial}{\partial y}(\rho v^2 + p) = 0, \tag{2.3}$$

$$u\frac{\partial s}{\partial x} + v\frac{\partial s}{\partial y} = 0, \tag{2.4}$$

where x and y are the streamwise and transverse spatial variables. Throughout this study, the positive x-axis will be aligned with the undisturbed free stream. Here u and v are the x and y Cartesian components of the velocity of a fluid particle. Equation (2.1) is recognized as the mass equation. Equations (2.2)–(2.3) are the x- and y-components of the momentum equation respectively, and equation (2.4) is the energy equation cast in terms of entropy.

In the numerical scheme presented here, we will simplify the system of equations (2.1)–(2.4) by replacing the energy equation (2.4) with the following algebraic equation:

$$\mathscr{H} = \mathscr{H}(V, T, u, v) = h + \tfrac{1}{2}(u^2 + v^2) = \mathscr{H}(V_\infty, T_\infty, u_\infty, v_\infty), \tag{2.5}$$

where $h = h(V, T) = e + pV$ is the enthalpy associated with a fluid element. Here $\mathscr{H}$ is referred to as the total enthalpy, $V \equiv \rho^{-1}$ is the fluid specific volume, T is the absolute

temperature, $e = e(V, T)$ is the internal energy, and the subscript ∞ denotes the value of the relevant quantity in the free stream. We recognize (2.5) as the Bernoulli equation for steady, compressible flow. As is well known, (2.5) holds across all stationary shock waves as well as the portions of the flow characterized by smooth transitions in thermodynamic properties. Since the free-stream conditions are assumed to be uniform, the value of $\mathscr{H}$ is a constant at every point in the flow field. We point out in §4 that (2.5) will be solved iteratively in conjunction with an equation of state. Because of the complexity of the equation of state used here, an iterative process would have been required in any case just to invert the equation of state. As a result, the additional iteration on the Bernoulli equation (2.5) causes no further complications in the actual implementation of the code.

Because the flow is assumed to be inviscid, the no-slip boundary conditions will not be applied, and the only remaining boundary conditions are the no-penetration conditions at the upper and lower surfaces. The result of these boundary conditions being imposed is that the particle velocity at the boundary is everywhere tangent to the surface. These boundary conditions may be expressed as

$$v = ub'_l \quad \text{at} \quad y = b_l \quad \text{and} \quad v = ub'_u \quad \text{at} \quad y = b_u, \tag{2.6}$$

where $b_l = b_l(x)$ is the function which describes the shape of the upper surface of the lower blade, $b_u = b_u(x)$ is the function associated with the shape of the lower surface of the upper blade. The prime denotes differentiation with respect to x.

The two independent thermodynamic variables, V and T, along with the two Cartesian velocity components may be determined from (2.1)–(2.3) and (2.5) subject to the boundary conditions (2.6). Because the flow is taken to be single phase at every point in the flow, all other thermodynamic parameters may be determined through use of the equation of state.

3. Scalings and curvilinear coordinates

Since the region in which the flow is to be analysed is non-rectangular, it will be convenient to introduce a coordinate transformation which maps the irregular physical domain into a rectangular computational domain. A sketch of the physical domain is provided in figure 6. Here we employ the following transformation:

$$\left. \begin{aligned} x &= x(\zeta) = \zeta L, \\ y &= y(\zeta, \eta) = \epsilon L h_l(\zeta) + (H + \epsilon L h_u(\zeta) - \epsilon L h_l(\zeta))\, \eta, \end{aligned} \right\} \tag{3.1}$$

where L is a measure of the characteristic length of the blades and H is a parameter associated with the spacing between the two surfaces. The resulting computational region is a dimensionless rectangle. Here h_l and h_u are dimensionless shape functions associated with the lower and upper surfaces respectively, and are related to b_l and b_u by

$$b_l(x) = \epsilon L h_l(\zeta) \quad \text{and} \quad b_u(x) = H + \epsilon L h_u(\zeta), \tag{3.2}$$

where ϵL is a measure of the half-thickness of the blades. No restrictions to the use of thin blades has been made. Therefore, the non-dimensional parameter ϵ may or may not be small.

After introducing the transformations (3.1) and the definitions (3.2), the equations describing the flow (2.1)–(2.3) and the accompanying boundary conditions (2.6) may be cast entirely in terms of the variables ζ and η. It will also be convenient to cast the
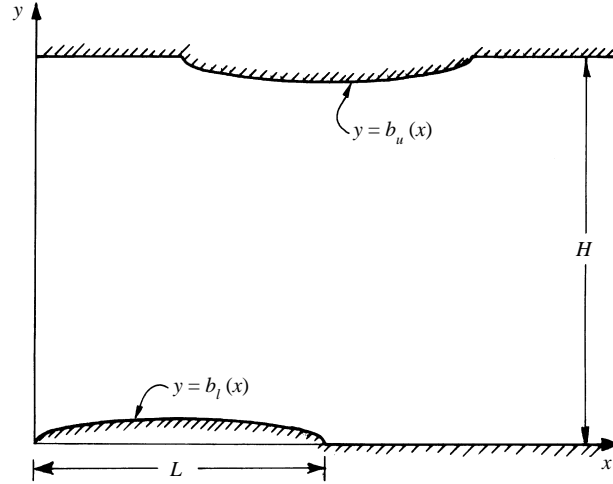
FIGURE 6. Sketch of the general physical domain.

equations entirely in terms of the following non-dimensional thermodynamic variables, denoted by an overbar:

$$V = \bar{V}V_c, \quad T = \bar{T}T_c, \quad p = \bar{p}p_c, \quad u = \bar{u}(RT_c)^{1/2}, \quad v = \bar{v}(RT_c)^{1/2},$$
$$e = \bar{e}RT_c + e_{ref}, \quad \mathscr{H} = RT_c\bar{\mathscr{H}} + e_{ref}, \quad x = \bar{x}L \equiv \zeta L, \quad y = \bar{y}H, \tag{3.3}$$

where R is the gas constant specific to the fluid of interest and e_{ref} is the internal energy associated with an arbitrary reference thermodynamic state. Here the subscript c refers to the value of the thermodynamic property evaluated at the thermodynamic critical point. After introducing the coordinate transformation (3.1) and the scalings (3.3), the system (2.1)–(2.3) may be recast as

$$\frac{\partial \boldsymbol{q}}{\partial \zeta} + \frac{\partial \boldsymbol{F}}{\partial \eta} = \boldsymbol{0} \tag{3.4}$$

subject to the boundary conditions

$$\bar{v} = \epsilon h_l' \bar{u} \quad \text{at} \quad \eta = 0, \quad \text{and} \quad \bar{v} = \epsilon h_u' \bar{u} \quad \text{at} \quad \eta = 1, \tag{3.5}$$

where the prime now denotes differentiation with respect to ζ. Here the vectors $\boldsymbol{q}$ and $\boldsymbol{F}$ are given by

$$\boldsymbol{q} = \boldsymbol{m}(H/L + \epsilon(h_u - h_l)), \quad \boldsymbol{F} = \boldsymbol{R} - \boldsymbol{m}\epsilon(h_l' + (h_u' - h_l')\eta), \tag{3.6}$$

where the vectors $\boldsymbol{m}$ and $\boldsymbol{R}$ are defined to be

$$\boldsymbol{m} = \left\{ \frac{\bar{u}}{\bar{V}}, \frac{\bar{u}^2}{\bar{V}} + Z_c\bar{p}, \frac{\overline{uv}}{\bar{V}} \right\} \quad \text{and} \quad \boldsymbol{R} = \left\{ \frac{\bar{v}}{\bar{V}}, \frac{\overline{uv}}{\bar{V}}, \frac{\bar{v}^2}{\bar{V}} + Z_c\bar{p} \right\}. \tag{3.7}$$

Here $Z_c \equiv p_c V_c / RT_c$ is the critical compressibility of the fluid.

4. Outline of numerical scheme

The governing equations are now in a form that is convenient to solve numerically. The entire thermodynamic state is known and is further assumed to be uniform along the line $\zeta = 0$. We choose to solve the system (3.4) with an explicit MacCormack differencing scheme because of the ease of implementation of the MacCormack scheme

and its ability to accurately capture shock waves. Complete details of its implementation may be found in the original article by MacCormack (1969) and most texts on computational fluid dynamics, e.g. Fletcher (1988).

The flow region is discretized into a set of distinct mesh points at which the flow is to be determined. A typical grid consists of 751 nodes in the ζ-direction by 251 nodes in the η-direction. The predictor stage of the MacCormack finite differencing scheme is implemented to obtain the values of the q-vector for all of the nodes at the next value of ζ = constant. The components of the m-vector are easily determined from the definitions in (3.6). Once the components of the m-vector are known at the predictor stage for each set of nodes corresponding to ζ = constant, it is necessary to determine the corresponding values of the temperature and specific volume at each of these grid points. This is done by solving the following algebraic system of equations which is simply composed of the expression for the total enthalpy (2.5), expressed in non-dimensional form, and an equation that relates the first two components of the m-vector to the thermodynamic variables. The resultant algebraic system that is solved is

$$\bar{e}+\frac{m_1^2\,\bar{V}^2+(m_3/m_1)^2}{2}+Z_c\bar{p}\bar{V}-\bar{\mathcal{H}}_\infty=0, \tag{4.1}$$

$$m_1^2\,\bar{V}+Z_c\bar{p}-m_2=0, \tag{4.2}$$

where m_i denotes the ith component of m. Since all of the components of m are known at this point and the flow is single phase, this is a system of two equations in two unknowns, $\bar{V}$ and $\bar{T}$. Once $\bar{V}$ and $\bar{T}$ have been determined, the other thermodynamic variables are easily determined from the explicit form of the gas model. After the thermodynamic variables are known at the predictor stage, the components of the Cartesian velocity vector are determined from

$$\bar{u}=m_1\,\bar{V} \quad \text{and} \quad \bar{v}=m_3/m_1, \tag{4.3}$$

from which the corresponding components of the R-vector may be determined. Once the components of R are known, the components of F are easily determined from the definitions in (3.6). The corrector and artificial viscosity stages of the MacCormack scheme are applied in the same manner as the predictor stage discussed here.

The boundary conditions imposed in the present study are an extension of Abbett's (1973) method for a perfect gas which is discussed in most texts on computational fluid dynamics, e.g. Fletcher (1988). The authors use the same general procedure except that these conditions are modified to allow for the use of the more general gas model discussed in the next section.

5. Gas model

A complete gas model is obtained by specifying the equation of state and the temperature dependence of the ideal gas or zero-pressure specific heat, defined as

$$c_{v\infty}=c_{v\infty}(T)=\lim_{V\to\infty}c_v(V,T). \tag{5.1}$$

In the present study, we choose a power law zero-pressure specific heat model, i.e. one of the form

$$c_{v\infty}=c_{v\infty}(T_{ref})\,(T/T_{ref})^n, \tag{5.2}$$

where n is a constant that is unique to the fluid of interest, and as before, the subscript *ref* corresponds to the property evaluated at an arbitrarily chosen reference state.

The equation of state that is used for determining the physical properties at each point in the flow field is that due to Martin & Hou (1955). This model is chosen for its relatively accurate description of the thermodynamic behaviour over the global range of pressures and temperatures encountered by a single-phase fluid as well as being relatively easy to implement in most numerical schemes. The general form of the Martin–Hou equation of state is

$$p = \frac{RT}{V-b} + \sum_{i=1}^{4} \mathcal{Q}_i \mathcal{F}'_i. \tag{5.3}$$

Here b is a constant measuring the excluded volume, and $\mathcal{Q}_i = \mathcal{Q}_i(T)$ and $\mathcal{F}_i = \mathcal{F}_i(V)$ are defined in the original article by Martin & Hou (1955). Throughout this section the prime will denote differentiation with respect to T or V as appropriate.

We should point out that (5.3) cannot account for critical point singularities in the transport properties which occur in a small neighbourhood of the thermodynamic critical point. Experience reveals that the general states of interest are well away from this near-critical regime. Furthermore, the near-critical effects simply tend to enhance the advantageous effects described here.

The corresponding expressions for the entropy and internal energy may be shown to be

$$s = s_{ref} + \phi_s + R \ln \left(\frac{V-b}{V_{ref}-b} \right) + \sum_{i=1}^{4} (\mathcal{Q}'_i \mathcal{F}_i - (\mathcal{Q}'_i \mathcal{F}_i)|_{ref}) \tag{5.4}$$

and

$$e = e_{ref} + \phi_e + \sum_{i=1}^{4} [\mathcal{F}_i(T\mathcal{Q}'_i - \mathcal{Q}_i) - \mathcal{F}_{iref}(T\mathcal{Q}'_i - \mathcal{Q}_i)|_{ref}] \tag{5.5}$$

respectively, where

$$\phi_s \equiv \int_{T_{ref}}^{T} \frac{c_{v\infty}}{T} dT \quad \text{and} \quad \phi_e \equiv \int_{T_{ref}}^{T} c_{v\infty} dT. \tag{5.6}$$

Complete details of the implementation of the Martin–Hou equation may be found in the original paper by Martin & Hou (1955), and further discussion of the specific heat in the present context may be found in Cramer (1989 *a*).

The vapour pressure is also calculated at each point in the flow field in order to ensure that the gas does not enter the two-phase region. The vapour pressure model is that due to Riedel (1954). At the end of every calculation, the values of the temperature and pressure at every point were compared to those of the vapour pressure curve. If any point in the flow is found to be in the two-phase region, the entire flow is discarded as invalid.

6. Recovery of classical results

As a check on our numerical scheme and our implementation of the gas model, we have carried out extensive comparisons to quasi-analytical solutions. Monaco (1994) has reported examples of our comparisons to cases involving perfect gas shock waves and Prandtl–Meyer expansion fans for nitrogen and carbon dioxide. Monaco clearly demonstrates that the use of the MacCormack scheme and Martin–Hou equation can routinely recover the classical perfect gas results.

In order to save space we will simply report the results of the generation and reflection of a compression shock in a dense gas. The specific case that is considered is the flow of steam (H_2O) past a $10°$ compression corner. The compression shock that
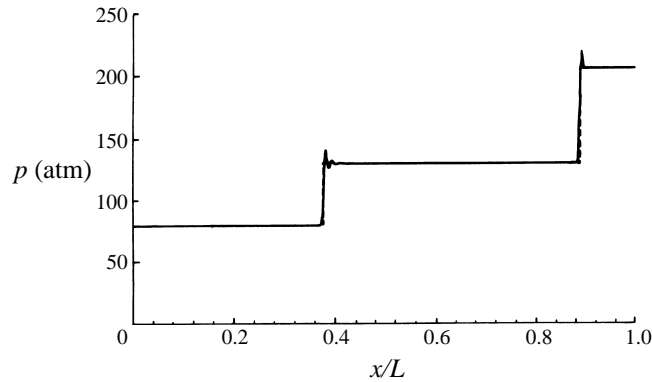
FIGURE 7. Pressure distribution for the reflection of an oblique shock in H_2O from a rigid wall located at a distance $L/2$ above the $y = 0$ axis. The flow deflection angle of the incident shock is 10°. The free-stream parameters correspond to $V_\infty = 10.0V_c$, $T_\infty = T_c \approx 647.3$ K, $p_\infty = 79.6$ atm, and $M_\infty = 2.0$. The numerical solution is given by the solid line, and the exact solution is given by the dashed line.

develops at the front of the wedge is reflected from a rigid wall located at a distance H above the $y = 0$ axis. Here the length scale, L, is taken to be twice the distance between the $y = 0$ axis and the rigid wall, i.e. $L = 2H$. The free-stream parameters for this case are $V_\infty = 10.0V_c$, $T_\infty = T_c \approx 647.3$ K, and $M_\infty = 2.0$. The corresponding pressure is 79.6 atm which is approximately 37 % of the critical value. Thus, dense gas effects are important at these temperatures and pressures. In figure 7 we compare the pressure increases from our numerical calculations to an exact solution computed by a technique similar to that employed by Cramer (1991*b*). The latter solution employs the exact shock jump relations for arbitrary gases combined with the Martin–Hou equation. A straightforward iterative scheme was employed to solve the resultant algebraic equations. Because of the shock angle geometries of both the incident and reflected shock, it is convenient to sample the pressure distribution at $y = 0.3L$. The numerical solutions based on the MacCormack scheme are plotted as a solid line and those based on a solution of the oblique shock relations are plotted as dashed lines. With the exception of the numerical oscillations at the shocks, we have good agreement between the dense gas solution and our approximate solution.

On the basis of this example, those reported by Monaco (1994), as well as many calculations which remain unpublished, we conclude that the numerical scheme combined with the Martin–Hou equation gives a reasonable representation of both perfect and dense gas flows.

7. Examples of shock disintegration

As pointed out in the Introduction, compression discontinuities inserted in BZT fluids may disintegrate either completely or partially. The purpose of this section is to provide numerical illustrations of the four modes by which compression discontinuities may disintegrate. We also demonstrate that a reasonable amount of spreading appears possible even when the disintegration of the compression discontinuity is incomplete.

Because no analytical solutions analogous to those of §6 are available, all results of the present section are numerical in nature. However, the results presented here appear to be completely consistent with the shock existence conditions discussed by Menikoff & Plohr (1989) and Cramer (1989*b*, 1991*a*), at least insofar as they could be checked. Because of the local equivalence between arbitrarily moving, arbitrarily oriented shock

waves and normal stationary shocks, the existence conditions developed in the previous investigations can be carried over immediately to the present case.

To illustrate the disintegration in as simple a manner as possible, we restrict our attention to an infinite wedge similar to that sketched in figure 5(a). In the numerical calculations the upper wall is taken to be parallel to the free stream, i.e. $b_u \equiv H$, and is placed far enough away from the lower wedge that reflected waves play no role in the wave evolution plotted here. In this section we take the characteristic length scale L to be the largest value of y at which we sample the pressures. The estimates of the spreading in the x-direction should then be compared to this transverse distance.

In order to better visualize the disintegration process, each of the plots have been shifted in the x-direction so that the origin coincides with the free-stream Mach line which originated at the beginning of the wedge at $(x, y) = (0, 0)$. Thus, when the wave system is headed by a centred fan, the non-zero portion of the disturbance should begin at $X = 0$. Here $X \equiv x - y(M_\infty^2 - 1)^{1/2}$ is the shifted x-variable. Because nearly all admissible shocks travel faster than the acoustic waves ahead of it, any shock waves will stand upstream of the free-stream Mach line emanating from the origin. Thus, shock waves will typically correspond to negative values of X. The only exceptions to this pattern are shocks having sonic conditions immediately upstream of the shock. In such cases, the position of such a shock will correspond to $X = 0$ in the shifted coordinate system. We should note that a pure sonic shock, whether an upstream or downstream sonic shock, only occur at a single flow deflection or wall wedge angle. At neighbouring flow deflection angles, the shock is either non-sonic or is adjacent to a smooth wave. The latter is a centred fan for the wedge boundary conditions employed in the present section. As a result, the occurrence of a free-standing sonic shock in most experiments or numerical simulations will be rare. In the results presented here, all sonic shocks are associated with a centred fan.

The first case considered is the flow of PP11 past a 10° compression corner. The free-stream conditions for this case correspond to a volume and a temperature of $2.1V_c$ and $0.99T_c \approx 643.6$ K respectively. The corresponding pressure was found to be $0.89p_c \approx 12.8$ atm. The free-stream Mach number was taken to be 1.5. These thermodynamic conditions correspond to a $\Gamma < 0$ state at a pressure between the local minimum of $\rho\Gamma/a$ and the low-pressure zero of Γ. The actual value of the free-stream fundamental derivative is $\tilde{\Gamma}_\infty = -0.10$. The computed pressure and $\tilde{\Gamma}$-distributions at various y-elevations are plotted in figures 8(a) and 8(b). Inspection of figure 8(b) reveals that the 10° turning angle is so small that the flow remains in the $\Gamma < 0$ region. As suggested by an inspection of (1.4), the compression discontinuity disintegrates completely. Furthermore, it is observed to spread at approximately a linear rate. With the exception of a small precursor due to the artificial viscosity employed in the numerical scheme, the front of the wave approximately coincides with the free-stream Mach line which originates at the nose of the wedge. These two observations along with more extensive tests not reported here are in marked contrast to those expected for a shock which has been smeared by artificial viscosity. In the case of such a shock, the thickness would remain fixed after some initial transition period, and the bulk of the wave would be located to the left of the $X = 0$ point. Finally, we note that the width of the compression wave is approximately 19% of the transverse, i.e. y, distance it has propagated. Compression fans of comparable width were predicted and computed in the context of an extended weak shock theory by Crickenberger (1991).

The second case considered corresponds to the same fluid and free-stream conditions as the first example but with a wedge angle equal to 15°. In this case the compression generated is strong enough to take the flow into the $\Gamma > 0$ region. The pressure and $\tilde{\Gamma}$-
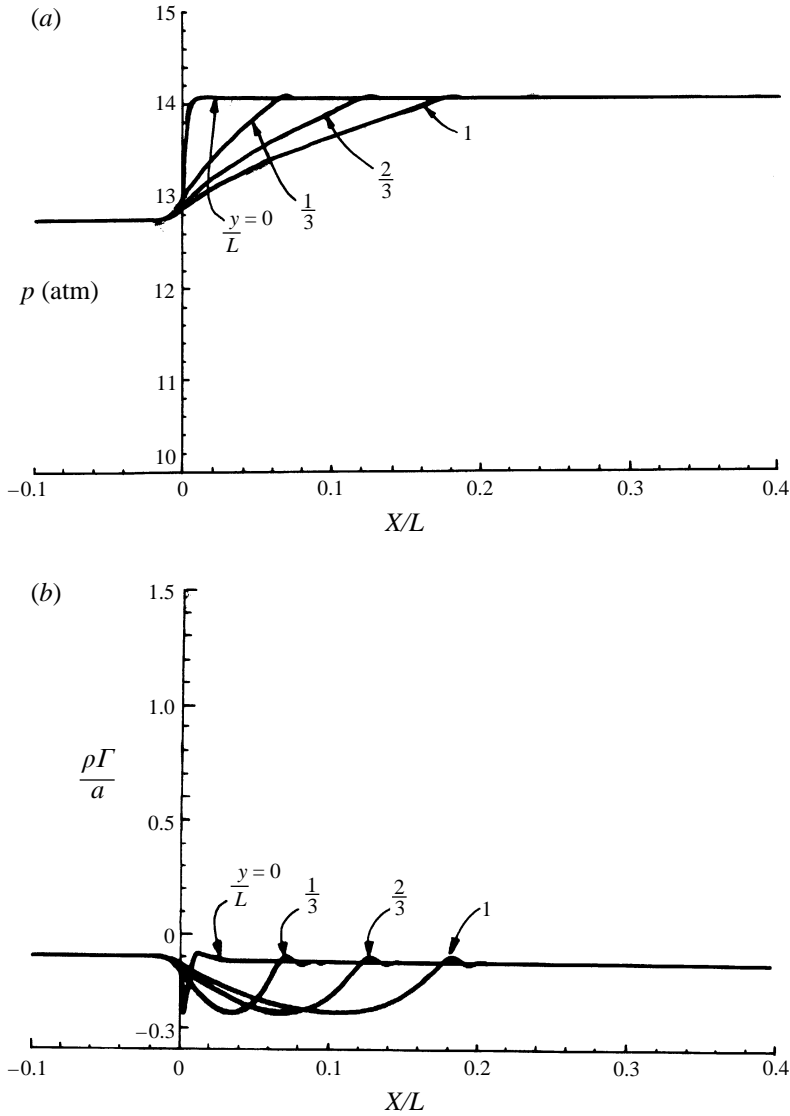
FIGURE 8. (*a*) Pressure distribution and (*b*) variation of $\rho \Gamma / a$ along various $y =$ constant lines for the flow of PP11 past a $10°$ compression corner. The free-stream conditions are $V_\infty = 2.1 V_c$, $T_\infty = 0.99 T_c \approx 643.6$ K, $p_\infty = 0.89 p_c \approx 12.8$ atm, and $M_\infty = 1.5$.

variations are plotted in figures 9(*a*) and 9(*b*). As discussed in §1, compression shocks are expected to form whenever the flow is compressed out of the $\Gamma < 0$ region. The configuration is therefore a compression fan followed by a compression shock. From a comparison of the $y = \frac{2}{3}L$ and $y = L$ cases, it is clear that the slightly smeared shock remains of constant thickness while the isentropic part of the compression continues to spread. Although the total compression is no longer isentropic, the overall compression is spread over approximately 12% of the propagation distance. In particular, only about 0.6 atm of the compression is in the form of a shock whereas the rest is distributed over a finite distance.

The wave constructions found in Menikoff & Plohr (1989), Kluwick (1991) and Cramer (1989*b*, 1991*a*) can be used to illustrate the change in the structure of the
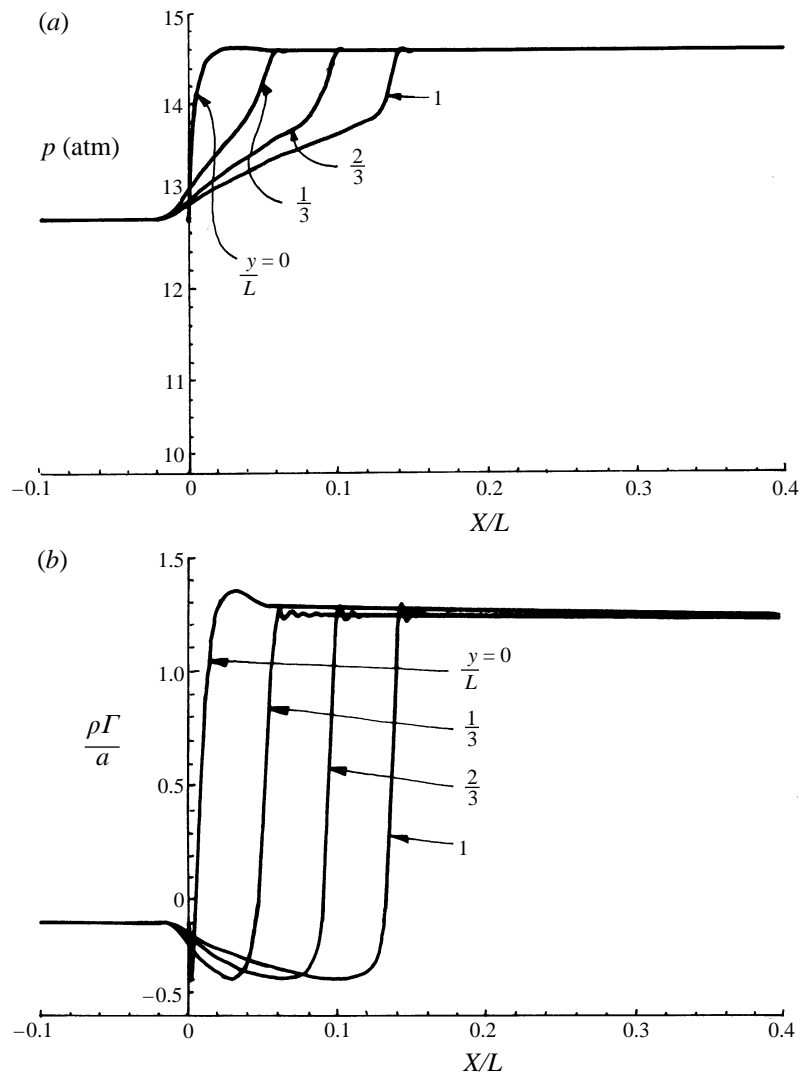
FIGURE 9. (*a*) Pressure distribution and (*b*) variation of $\rho\Gamma/a$ along various y = constant lines for the flow of PP11 past a 15° compression corner. The free stream conditions are identical to those of figure 8.

fan–shock system which occurs as the wedge angle is increased further. It may be shown that the shock increases in strength and moves forward in the fan. Ultimately, the shock reaches the first Mach wave of the fan and, at this stage, the fan thickness has shrunk to zero and the entire compression occurs through the shock. At larger wedge angles, the shock slope is larger than that of the free-stream Mach line and the shock is seen to move into the $X < 0$ region.

In the next example, the fluid is FC-71 which flows over a 15° wedge. The free-stream Mach number, specific volume, temperature, and pressure were taken to be $M_\infty = 1.6$, $V_\infty = 2.7V_c$, $T_\infty = 0.992T_c \approx 641$ K, and $p_\infty = 0.81p_c \approx 7.5$ atm. The scaled version of the free-stream fundamental derivative was found to be $\tilde{\Gamma}_\infty = 0.24$. This free-stream thermodynamic state was chosen so that any compression, either along a shock adiabat or along an isentrope, results in downstream states which approach the $\Gamma < 0$ region.
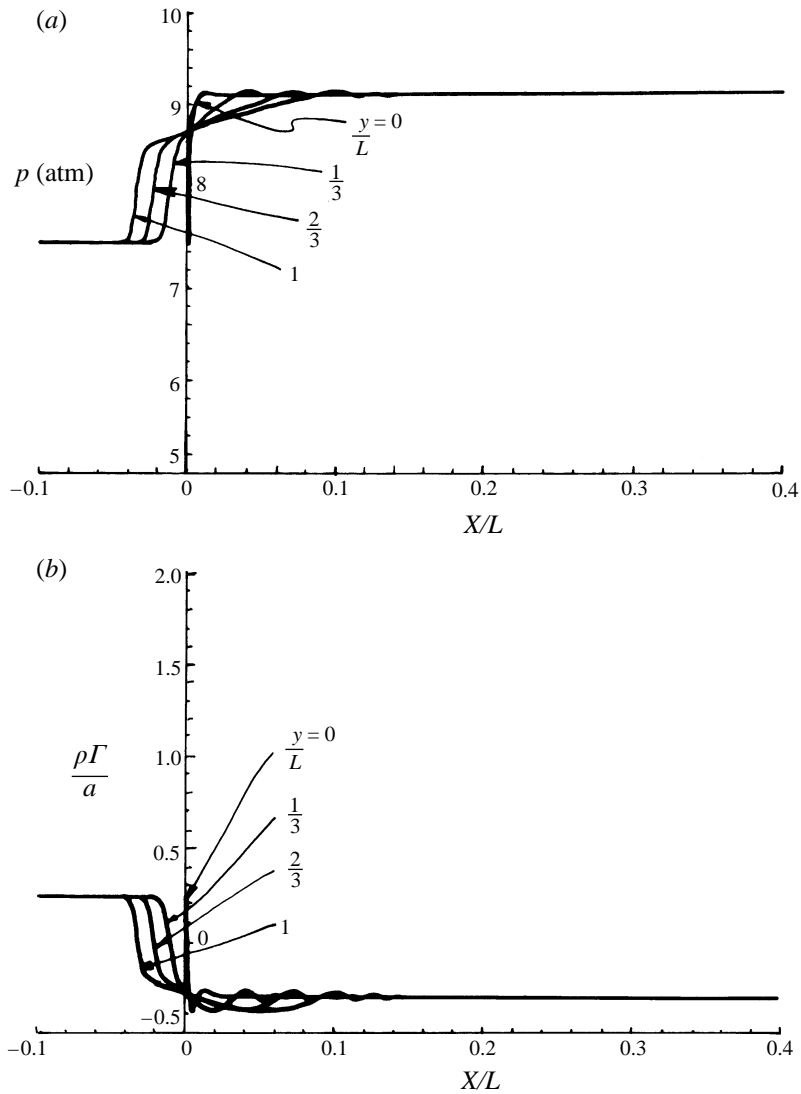
FIGURE 10. (*a*) Pressure distribution and (*b*) variation of $\rho\Gamma/a$ along various $y = $ constant lines for the flow of FC-71 past a 15° compression corner. The free-stream conditions are $V_\infty = 2.7V_c$, $T_\infty = 0.992T_c \approx 641$ K, $p_\infty = 0.81p_c \approx 7.5$ atm, and $M_\infty = 1.6$.

For sufficiently small wedge angles, the compression discontinuity can remain intact as a shock, even if the downstream state corresponds to $\Gamma < 0$. Again, the reader is referred to the work of Menikoff & Plohr (1989), Kluwick (1991) and Cramer (1989*b*, 1991*a*) for a discussion of the fundamental existence issues. However, for the 15° wedge chosen here, the flow is compressed so far into the $\Gamma < 0$ region that the discontinuity is inadmissible and therefore undergoes a partial disintegration into a shock–fan combination. The pressure and $\tilde{\Gamma}$-variations for this case are plotted in figures 10(*a*) and 10(*b*). We also note that this case is qualitatively the same as that sketched in figure 5. Inspection of figure 10(*a*) reveals that the overall compression is spread over approximately 13 % of the distance propagated. The remaining shock is approximately 60 % of the total compression.

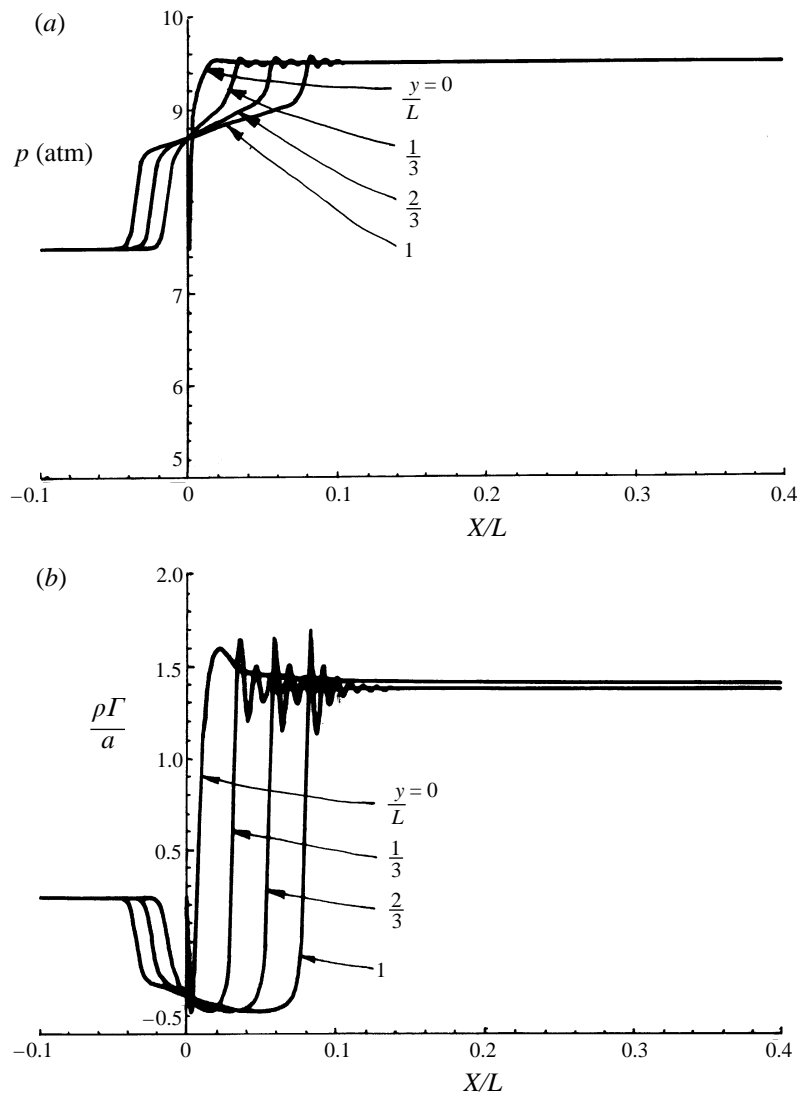The fourth example uses the same fluid (FC-71) and the same free-stream conditions

FIGURE 11. (*a*) Pressure distribution and (*b*) variation of $\rho\Gamma/a$ along various $y = $ constant lines for the flow of FC-71 past a 20° compression corner. The free stream conditions are identical to those of figure 10.

as in the previous example. The only change is that the wedge angle has been increased to 20°. The resultant pressure and $\tilde{\Gamma}$-distributions have been plotted in figures 11(*a*) and 11(*b*). The discontinuity generated remains inadmissible, but the flow has been compressed all the way through the $\Gamma < 0$ region and into the high-pressure $\Gamma > 0$ region. As discussed in the Introduction the compression fan then folds over on itself and the second shock seen in figure 11(*a*) necessarily appears. Because of the appearance of multiple shocks, this configuration was referred to as shock-splitting in the Introduction. Again we find that the total compression is distributed over a finite distance; in this case the spreading is about 11 % of the propagation distance. Several steady-flow, split-shock configurations were also computed by Crickenberger (1991), albeit for the case of weak shocks.

We note that the formation of the second shock in this last case is due to the same mechanism as discussed in the case depicted in figure 9. The variation of the pressure distributions seen as the wedge angle increases also follows the same pattern as discussed for the case corresponding to figure 9. That is, the strength of the second shock increases and moves forward through the fan until the fan disappears and the second shock merges with the first. At wedge angles exceeding the value corresponding to merger, the initial compression discontinuity is admissible and the complete compression is again through a shock wave. A sequence corresponding to that depicted in figures 5, 10 and 11 is found in the articles by Cramer (1989*b*, 1991*a*) for the case of one-dimensional unsteady flows.

Inspection of figure 11 reveals that the numerical oscillations in the fundamental derivative behind shocks can be proportionally larger than those for the pressure. This observation can be understood by recognizing that the wave system depicted in figure 11 takes the flow from the low-pressure, low-density side of the region of $\Gamma < 0$ to the high-pressure, high-density side of this region. Because the flow is nearly isothermal when BZT fluids are employed, figure 2 gives a reasonable picture of the qualitative variation of $\rho\Gamma/a$. Inspection of this figure reveals that small changes in density, and, it turns out, pressure, will lead to large changes in $\rho\Gamma/a$. Thus, one should always expect that the numerical oscillations will be somewhat larger for Γ than for the pressure when the downstream state is in the region of rapidly changing Γ.

We conclude this section by noting that complete and partial disintegrations of compression discontinuities can result in significant spreading of the compression wave. Although we have illustrated the disintegration process using compressions on the order of one or two atmospheres, Crickenberger (1991) has demonstrated that each mode of disintegration is possible within the context of his extended weak shock theory. However, the larger-amplitude waves are likely to result in greater spreading due to the larger difference in the slopes of the Mach lines.

8. Results

In this section we present examples of the flow of BZT fluids through the cascade configurations discussed in the Introduction. To begin, we compare the flow of steam (H_2O) and FC-71 ($C_{18}F_{39}N$) corresponding to identical free-stream conditions between two sinusoidal blades. We choose steam as the gas for comparison because of its widespread use as a working fluid in turbomachinery applications. The equations for the lower and upper blades are given by

$$b_l(x) = \begin{cases} \epsilon L \sin(\pi x/L) - L(x/L)\tan\theta_a, & 0 \leqslant x/L \leqslant 1 \\ -L\tan\theta_a, & 1 < x/L \leqslant 2, \end{cases} \tag{8.1}$$

and

$$b_u(x) = \begin{cases} H, & 0 \leqslant x/L < s/L \\ H - \epsilon L \sin(\pi(x-s)/L) - L[(x-s)/L]\tan\theta_a, & s/L \leqslant x/L \leqslant 1+s/L \\ H - L\tan\theta_a, & 1+s/L < x/L \leqslant 2, \end{cases}$$

$$\tag{8.1}$$

respectively. The computational domain extends from $x = 0$ to $x = 2L$ where the quantity L is now taken to be the chord of the blade and ϵL is the half-thickness of the blade. Here θ_a is the angle of attack, and s is the parameter associated with the staggering between the blades. Because our interest is in the nature of the compression
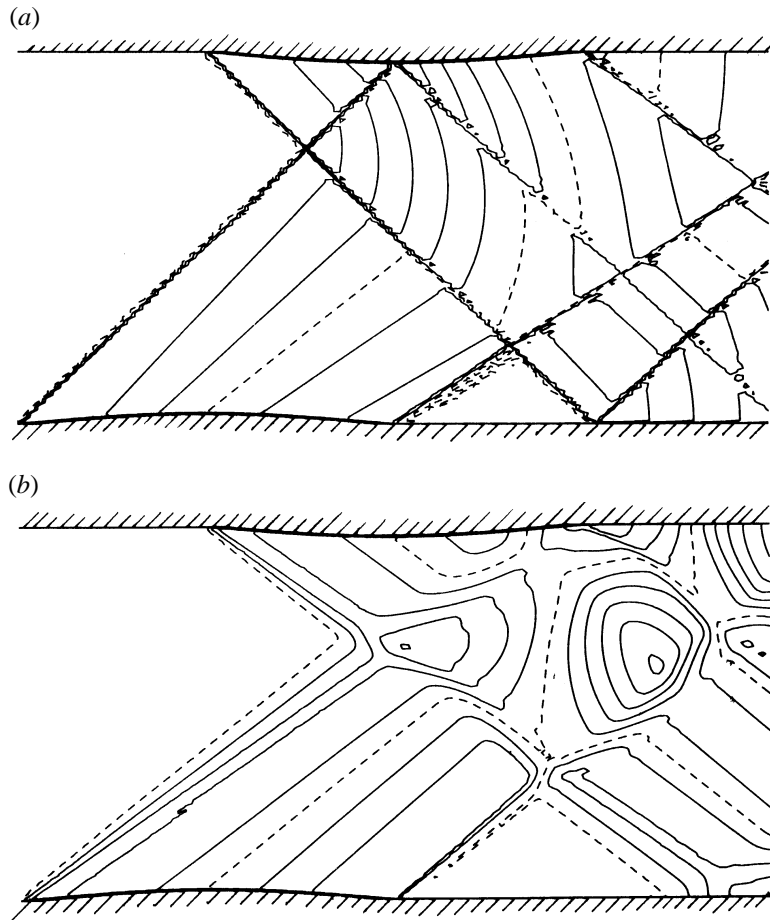
(*a*)

(*b*)

FIGURE 12. Constant c_p contours for the flow of (*a*) steam and (*b*) FC-71 between two staggered sinusoidal blades. The dashed line denotes $c_p = 0$, and each contour corresponds to a change in c_p of 0.05. The free-stream conditions are $p_\infty = 8.73$ atm, $T_\infty = 642.92$ K, and $M_\infty = 1.6$. The blade parameters are $\epsilon = 0.03$, $\theta_a = 0°$, and $s = 0.5L$.

waves which reflect from the blade surfaces, the stagger, s, and the Mach number are chosen such that the compression wave from the leading edge of the lower blade strikes the upper blade. Throughout this section we choose the spacing between the blades to be equal to one chord length, i.e. $H = L$.

In our first example, we take $\epsilon = 0.03$, $\theta_a = 0°$, and $s = 0.5L$, and we choose the free-stream conditions so that steam and FC-71 have identical pressures, temperatures, and Mach numbers in the undisturbed state. The free-stream parameters are a pressure of 8.73 atm, a temperature of 642.92 K, and a Mach number of 1.6. Because the critical pressure for steam is approximately 218 atm, steam behaves roughly as a perfect gas at these conditions. We note that one could also match the reduced pressure and temperatures or the reduced specific volume and temperature. However, steam will always have $\Gamma > 0$ and the compression shocks formed at the leading edge of the lower blade will always remain intact, leaving our primary results unchanged. Furthermore, comparisons based on the actual temperature and pressure are likely to be more meaningful if our results are to be evaluated in the context of overall Rankine cycle design.
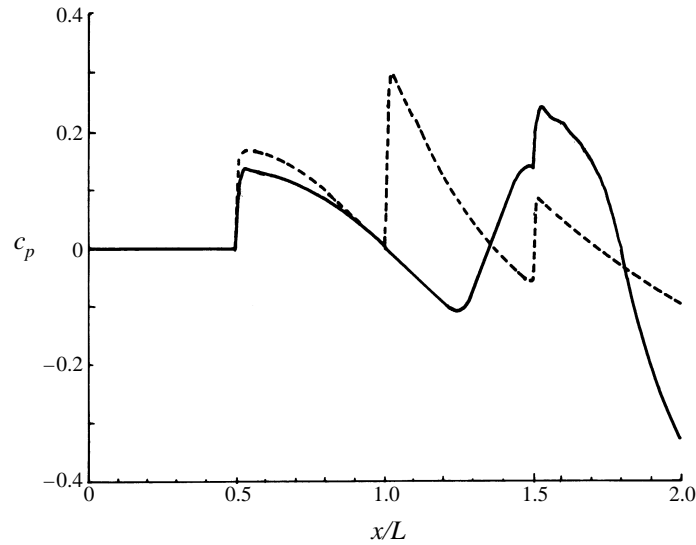
FIGURE 13. Variation in c_p along the upper wall for steam (dashed line) and FC-71 (solid line). The free-stream conditions and blade parameters are identical to those of figure 12. The leading edge of the upper blade is located at $x = L/2$.

In figure 12(a) the constant c_p contours for steam are plotted, and in figure 12(b) the corresponding c_p contours for FC-71 are shown. Here c_p is the usual coefficient of pressure defined as

$$c_p \equiv \frac{p - p_\infty}{\frac{1}{2}\rho_\infty U_\infty^2} = \frac{p - p_\infty}{\frac{1}{2}\rho_\infty a_\infty^2 M_\infty^2}, \tag{8.3}$$

where U_∞ is the free-stream flow speed. In the second expression, we have recast c_p in terms of the speed of sound and Mach number in the free stream. In figure 12 the contour corresponding to $c_p = 0$ is given by a dashed line, and each contour level corresponds to a change of 0.05 in the coefficient of pressure.

In figure 12(a) we note that for the case of steam there are clearly defined compression shocks emanating from both the leading and trailing edges of the blades and regions of smooth expansion are observed between these shocks. Here the results are in complete accord with classical theory. However, in figure 12(b) we notice that for FC-71 the leading-edge disturbances spread noticeably as they propagate into the flow. Furthermore, there appears to be no focusing of the lower-blade Mach lines after the intersection with the wave system coming from the upper blade. The compression emanating from the trailing edge of the lower blade appears to be a narrow compression fan, and this observation is consistent with the observed value of $\tilde{\varGamma}$ which was found to range from -0.13 to -0.44 as the flow passes the trailing edge. As we discuss later, we believe that the wave emanating from the trailing edge of the upper blade is initially either a shock or a fan–shock combination.

In figure 13 we plot the variation in c_p along the upper boundary. Here, the data for steam are given by a dashed line whereas the distribution for FC-71 is given by a solid line. In the case of steam, the reflection of the compression shock originating at the leading edge of the lower blade from the upper blade occurs at $x \approx L$ and is easily recognized as a discontinuity in figure 13. In the same figure, the reflection of the compression fan seen in figure 12(b) occurs in the region $1.25L < x < 1.5L$. Thus the
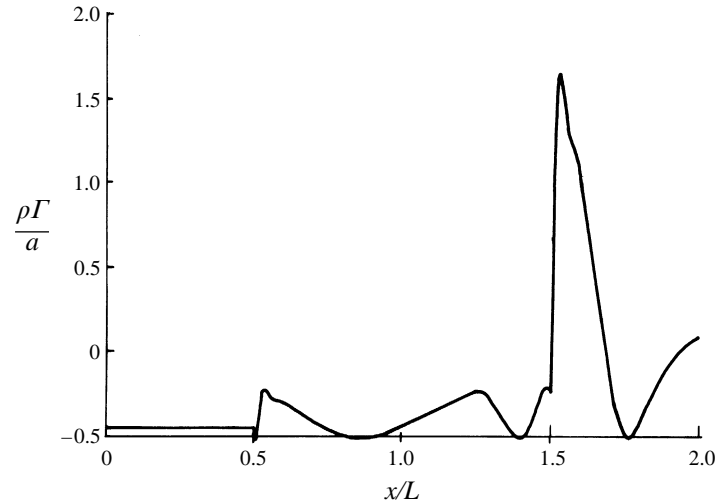
FIGURE 14. Variation in $\rho\Gamma/a$ along the upper wall for FC-71. The free-stream conditions and blade parameters are identical to those of figure 12. The leading edge of the upper blade is located at $x = L/2$.

compression fan in FC-71 survives the interaction between the two families of Mach waves and results in a reflected compression which extends over approximately 25% of the chord of the upper blade. This observation appears to be completely consistent with the discussion of the contour plot for FC-71. In contrast, the corresponding disturbance in steam is clearly a shock wave. On the basis of this comparison we conclude that the natural dynamics of BZT fluids, in this case FC-71, serve to spread the compression striking the upper blade over a significant fraction of the chord, thereby eliminating the strong adverse pressure gradient present in the case of steam.

On the basis of linear simple-wave theory, we would expect the variation of c_p near the leading edge to be identical for the two fluids considered, provided the blade shapes are identical. The difference between the steam and FC-71 distributions seen in the range $0.5L < x < L$ in figure 13 is due to the differences in the entropy rise between the two compressions. It is easily verified that the entropy rise through the shock generated in steam should result in slightly larger values of c_p than the isentropic variation present in FC-71.

An inspection of figure 13 also reveals that the impact points of the two compression waves on the upper surface are different by about one-third of a chord. Similar effects have been observed by the authors in other calculations and blade configurations not reported here. This is due to the strong refraction of the compression wave as it passes through the wave system emanating from the upper blade. The observation that the average Mach angle in the fan decreases is due to the fact that the Mach number increases through the compression originating at the leading edge of the upper blade. This, of course, contrasts with the classical theory where $\tilde{\Gamma} > 1$ and the Mach number necessarily decreases with increasing pressure. Such increases in the Mach number with increasing pressure were discussed in detail by Cramer (1991*a*) and Cramer & Best (1991), but were intrinsic in the earlier work of Thompson (1971).

In figure 14 we plot the values of $\tilde{\Gamma}$ along the upper boundary for FC-71. The case of steam is not included because the value of $\tilde{\Gamma}$ is found to be 1.14 in the free stream and remains essentially constant throughout the entire flow field. In figure 14 we see that $\tilde{\Gamma}$ is negative over the entire upper blade, becoming positive only at the trailing
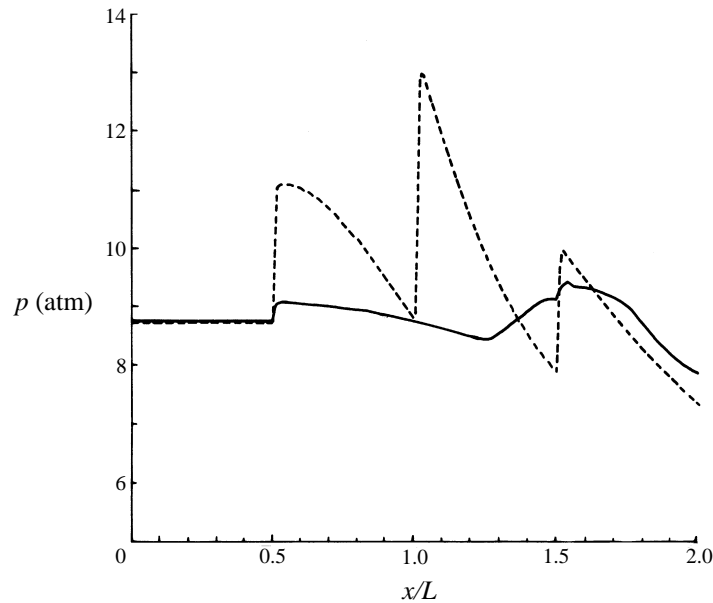
FIGURE 15. Actual pressures along the upper wall for steam (dashed line) and FC-71 (solid line). The free-stream conditions and blade parameters are identical to those of figure 12. The leading edge of the upper blade is located at $x = L/2$.

edge. The fact that $\tilde{\Gamma}$ remains negative across the leading edge is consistent with our earlier claim that the wave emanating from the leading edge is a compression fan rather than a shock. The trailing-edge disturbance from the upper blade corresponds to a change in sign of $\tilde{\Gamma}$ and is therefore either a compression shock or a fan–shock similar to that seen in figure 9(*a*).

Further examination of the flow suggests that the interaction of the smooth expansion emanating from the lower blade with the trailing edge compression shock from the upper blade tends to spread out the latter disturbance as it propagates into the flow. This is because the smooth expansion brings the flow state back into the $\Gamma < 0$ regime. This spreading is clearly evident in the contours plotted in figure 12(*b*).

The actual pressures for steam and FC-71 along the upper blade are plotted in figure 15. As before, the pressure distribution for steam is given by a dashed line, and that of FC-71 is given by a solid line. The main point to note here is that the overall change in pressure associated with FC-71 is several factors less than that of steam. The reason for this difference is revealed once we recall that linear theory predicts that the pressure coefficient (8.3) will be identical for any pair of fluids flowing over the same obstacle at the same free-stream Mach number. However, the value of $\rho_\infty a_\infty^2$ is considerably smaller for FC-71 than the corresponding value for steam. Because the free-stream pressures are identical, it is convenient to use the non-dimensional ratio $\rho_\infty a_\infty^2 / p_\infty$ to compare the two fluids. As a specific example we note that the actual value of $\rho_\infty a_\infty^2 / p_\infty$ is approximately 1.29 in the case of steam and approximately 0.25 in the case of FC-71. This difference in the actual pressure jumps further supports the claim that steam is more likely to lead to boundary layer separation than FC-71 when the two gases are operating at identical flow conditions.

It should be noted that any advantages due to the decrease in pressure levels is not due to the unique characteristics of BZT fluids. Both the decrease in pressure levels for a given Mach number and geometry and the occurrence of regions of $\Gamma < 0$ are due to
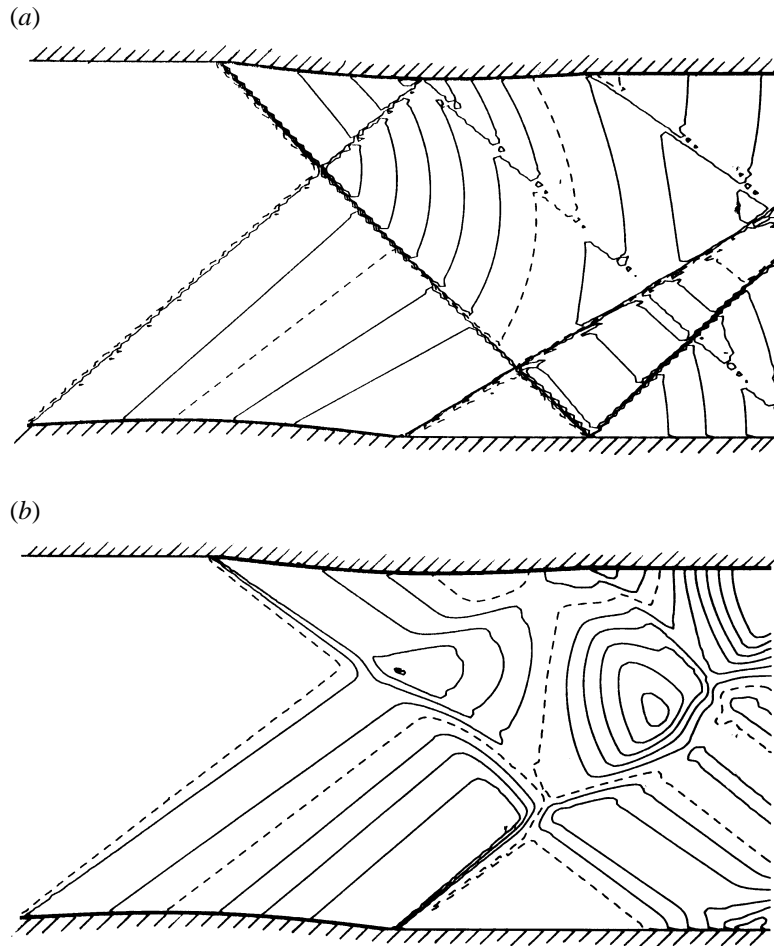
(*a*)

(*b*)

FIGURE 16. Constant c_p contours for the flow of (*a*) steam and (*b*) FC-71 between two staggered sinusoidal blades. The dashed line denotes $c_p = 0$, and each contour corresponds to a change in c_p of 0.05. The free-stream conditions are $p_\infty = 8.73$ atm, $T_\infty = 642.92$ K, and $M_\infty = 1.6$. The blade parameters are $\epsilon = 0.03$, $\theta_a = 1.7°$, and $s = 0.5L$.

the reduction of the sound speed in the dense gas regime. This decrease in the sound speed is particularly pronounced when fluids having large specific heats are considered. However, the decrease in sound speed, and ultimately the decrease in the $\rho_\infty a_\infty^2$ factor seen in (8.3), occurs for most fluids including those which are not BZT fluids. Of course, fluids with specific heats which are large enough to produce BZT effects also have reduced values of the $\rho_\infty a_\infty^2$ factor.

In our second example, we again compare the behaviour of steam to that of FC-71 using the same free-stream conditions as in the previous example, but we now consider blades at an angle of attack. The equations of the lower and upper blades are again given by (8.1) and (8.2) respectively. As before we take $\epsilon = 0.03$ and $s = 0.5L$, but now we choose the angle of attack to be $\theta_a = 1.7°$. Again the spacing between the two blades is taken to be one chord length. In figure 16(*a*) we plot the contours for steam and in figure 16(*b*) we plot the contours for FC-71. Again the contour corresponding to $c_p = 0$ is given by a dashed line and each successive contour corresponds to a change in c_p of 0.05. We note that the results are similar to the previous example except that
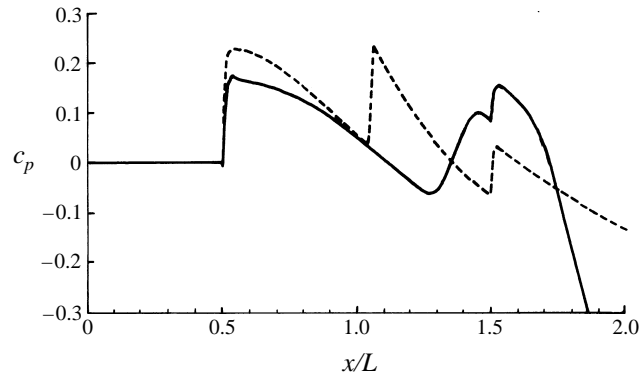
FIGURE 17. Variation in c_p along the upper wall for steam (dashed line) and FC-71 (solid line). The free-stream conditions and blade parameters are identical to those of figure 16. The leading edge of the upper blade is located at $x = L/2$.
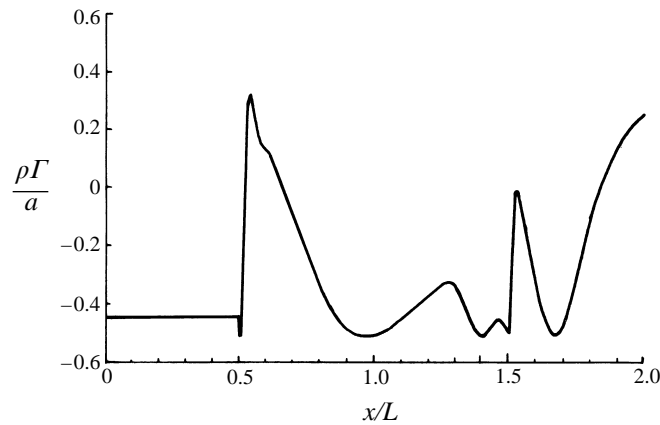

FIGURE 18. Variation in $\rho\Gamma/a$ along the upper wall for FC-71. The free-stream conditions and blade parameters are identical to those of figure 16. The leading edge of the upper blade is located at $x = L/2$.

now, because of the non-zero angle of attack, the leading-edge disturbance associated with the upper blade is stronger and the leading-edge disturbance from the lower blade is weaker. In the case of steam we still note very definite shock waves emanating from the leading edges of both the lower and upper surfaces, whereas in the case of FC-71, the leading-edge disturbances still exhibit noticeable spreading as these compression waves propagate into the flow.

In figure 17 we plot the coefficients of pressure for steam and FC-71 along the upper surface. We see that the leading-edge compression associated with the upper blade is indeed stronger than that in the previous example. The compression wave from the lower blade incident on the upper boundary is still a shock wave in the case of the steam and a compression fan in the case of FC-71. In the latter the compression is spread over approximately 20% of the chord length.

In figure 18 we plot the variation in $\tilde{\Gamma}$ for FC-71 along the upper surface. As before, the value of $\tilde{\Gamma}$ for steam remains essentially constant at a value of 1.14 throughout the flow field, and therefore is omitted. The variation of $\tilde{\Gamma}$ along the upper blade in the case
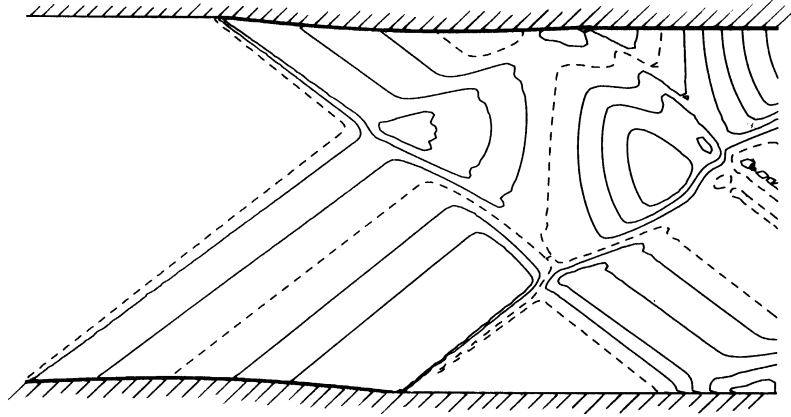
FIGURE 19. Constant c_p contours for the flow of PP11 between two staggered sinusoidal blades. The dashed lines denotes $c_p = 0$, and each contour corresponds to a change in c_p of 0.05. The free-stream conditions are $p_\infty = 13.25$ atm, $T_\infty = 655.9$ K, and $M_\infty = 1.6$. The blade parameters are $\epsilon = 0.025$, $\theta_a = 1.4°$, and $s = 0.5L$.

of FC-71 is consistent with the fact that the leading-edge compression emanating from the upper blade is stronger. In the previous example we noted that $\tilde{\Gamma}$ remained negative through the leading-edge compression wave. However, in the present example $\tilde{\Gamma}$ changes sign across the leading edge, which suggests that the wave system originating at the leading edge of the upper blade is a compression fan followed by a weak compression shock similar to that shown in figure 9(*a*). However, this shock is not readily visible in the contours owing to the resolution. Another interesting difference to note is that the disturbance at the trailing edge of the upper blade that was seen to be a shock in the previous example is now a pure compression fan. This follows by inspection of figure 18 where it is seen that $\tilde{\Gamma}$ is entirely negative across the trailing-edge compression wave.

In conclusion we have shown that the advantages of BZT fluids described in the first example of this section are also realized in lifting configurations. In retrospect, one might have anticipated that a small angle of attack would have little influence on the wave that arrives at the upper blade. The compression wave originating at the leading edge of the lower blade is weaker due to the angle of attack. However, this weakened wave undergoes a larger change due to its interaction with the strengthened compression emanating from the leading edge of the upper blade. The final result is a compression fan of approximately the same width and strength as that observed in the non-lifting example.

In our final example we consider the flow of PP11 between two staggered sinusoidal blades at an angle of attack to provide an example of an isentropic cascade. The equations of these surfaces are again given by (8.1) and (8.2), and now we choose $\epsilon = 0.025$, $s = 0.5L$, and $\theta_a = 1.4°$. The spacing between the two blades is still taken to be one chord length. The free-stream conditions are now taken to be $V_\infty = 1.84V_c$, $T_\infty = 0.992T_c \approx 644.9$ K, $p_\infty = 0.92p_c \approx 13.25$ atm, and $M_\infty = 1.6$. The corresponding value of (1.3) was found to be $\tilde{\Gamma}_\infty = -0.29$. In figure 19 we plot the contours of constant c_p. As in our previous two examples the contour corresponding to $c_p = 0$ is given by a dashed line, and the contours are equally spaced in increments of 0.05.

In figure 20(*a*) we plot the coefficient of pressure along the lower blade, and in figure 20(*b*) we plot the corresponding $\tilde{\Gamma}$-values. The distribution of the coefficient of pressure along the upper blade is given in figure 21(*a*), and the associated values of $\tilde{\Gamma}$ are plotted
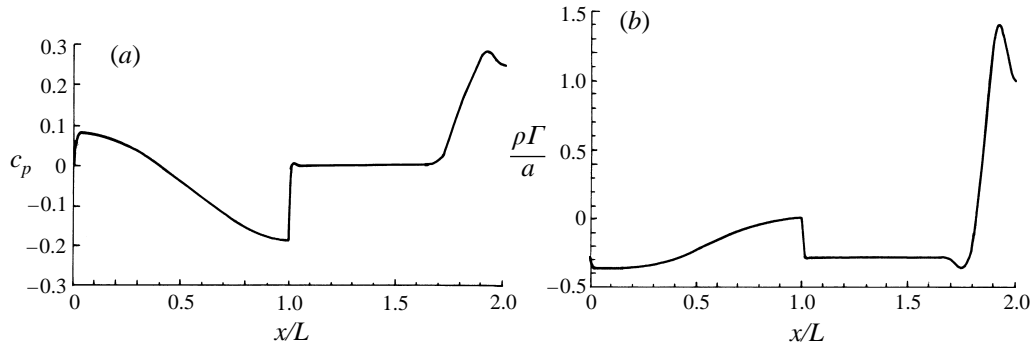
FIGURE 20. (a) Variation in c_p and (b) variation in $\rho\Gamma/a$ along the lower wall for PP11. The free-stream conditions and blade parameters are identical to those of figure 19. The leading edge of the lower blade is located at $x = 0$.
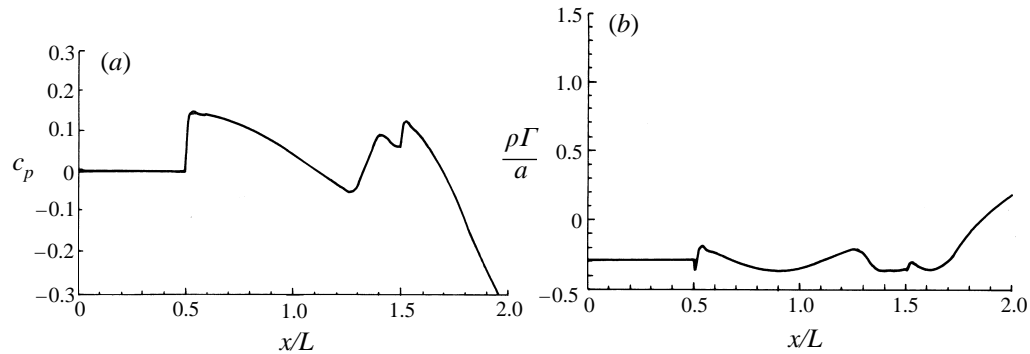

FIGURE 21. (a) Variation in c_p and (b) variation in $\rho\Gamma/a$ along the upper wall for PP11. The free-stream conditions and blade parameters are identical to those of figure 19. The leading edge of the upper blade is located at $x = L/2$.

in figure 21(b). From figure 20(b) we note that $\tilde{\Gamma}$ is negative along the entire length of the lower blade, indicating that both the leading-edge and trailing-edge disturbances are pure compression fans. In figure 21(b) we note that the value of $\tilde{\Gamma}$ is also negative along the entire upper blade which lies in the interval $L/2 \leqslant x \leqslant 3L/2$. Therefore, both the leading- and trailing-edge disturbances are pure compression fans with a smooth expansion between these fans. In figure 21(a) it can be seen that the leading-edge compression from the lower blade is spread over approximately 13% of a chord by the time it strikes the upper blade.

Because $\tilde{\Gamma}$ is negative across the entire lower blade, we would expect the smooth expansion to eventually form an expansion shock if it were allowed to propagate far enough away from the lower boundary. However, in figure 21 we see that by the time the expansion from the lower blade strikes the upper boundary, it is still spread over 50% of a chord length. This expansion is located in the range $1.5L < x < 2.0L$ in figure 21(a). Therefore, the space between the blades is not sufficient for the expansion shock to form. Furthermore, the contours presented in figure 19 show no steepening which would suggest shock formation of any kind in the neighbourhood of the blades.

On the basis of the data plotted here and more extensive checks on the numerical details of the flow between the upper and lower blades, we conclude that the entirely

isentropic cascade is possible even when the complications arising from the finite extent of the $\Gamma < 0$ region and the interactions between the two families of Mach waves are considered. Although this result is relatively straightforward to accomplish for non-lifting configurations, the example presented here demonstrates that fully isentropic cascades are also easily obtained in lifting configurations.

9. Summary

The present study should be considered a first step toward understanding the dense gas behaviour of Bethe–Zel'dovich–Thompson fluids in supersonic cascade configurations. We have verified the predictions originally made by Cramer (1991 *a*) who argued that the strong adverse pressure gradients associated with the reflection of compression shocks at neighbouring turbine blades can be significantly reduced if BZT fluids are employed. In particular, we have shown that the region of compression associated with these reflections can be spread over approximately 10–20 % of the blade chord. This contrasts with the behaviour of perfect gases where the reflection is accomplished at a point, at least in the inviscid theory. The advance over Cramer's work is that the finite extent of the $\Gamma < 0$ region is taken into account with an accurate equation of state. Furthermore, the complicated interactions between the Mach waves originating at the upper and lower blades have also been taken into account. The main result here is to demonstrate that the incoming inviscid signal is of finite spatial extent. However, the authors feel that this reduction in strength of the adverse pressure gradient reduces the likelihood of shock-induced separation. The triple-deck analysis of Kluwick (1994) and the Navier–Stokes computations of Cramer, Park & Watson (1996) appear to bear this intuitive claim out. Further results on our Navier–Stokes computations will be presented at a later time.

A second result of interest is the verification of the prediction of the existence of lifting, supersonic cascade flows which are entirely isentropic. This demonstration of shock-free supersonic flows is possible because compression shocks naturally disintegrate to form isentropic compression fans when $\Gamma < 0$ everywhere in the flow. Furthermore, the distance between neighbouring blades is not sufficient for expansion shocks associated with negative values of $\tilde{\Gamma}$ to form. Because such flows also have significantly reduced adverse pressure gradients, it may be possible to eliminate both boundary layer separation and shock irreversibility, resulting in an entirely loss-free supersonic cascade. An important observation is that all of these advantages are due to the natural dynamics of BZT fluids and are not dependent on special choices for the blade cross-sections.

In order to obtain the most pronounced advantageous effects, the authors believe that a free-stream state corresponding to a local minimum in $\tilde{\Gamma}$ should be chosen. By choosing such a free-stream state and by limiting the excursions outside the negative-$\tilde{\Gamma}$ region, it is possible to obtain the maximum spreading of compression waves by the time these waves reach neighbouring blades.

If one wishes to obtain a fully isentropic cascade, a free-stream state near the local minimum of $\tilde{\Gamma}$ still appears desirable. However, flows having strong negative nonlinearity, i.e. $\tilde{\Gamma} < 0$, increase the likelihood that an expansion shock can form in the distance between the blades. Because the physical mechanism leading to the spreading of compression discontinuities is the same as that leading to the formation of expansion shocks, a trade-off position will generally be sought. The examples presented here demonstrate that this can be accomplished fairly easily with practical blade configurations.

REFERENCES

ABBETT, M. J. 1973 Boundary condition calculation procedures for inviscid supersonic flow fields. In *Proc. 1st AIAA Computational Fluid Dynamics Conference, Palm Springs, California*, pp. 153–172.

ANDERS, J. B. 1993 Heavy gas wind-tunnel research at Langley Research Center. *ASME Paper* 93-FE-5.

ANDERSON, W. K. 1991*a* Numerical study of the aerodynamic effects of using sulfur hexafluoride as a test gas in wind tunnels. *NASA Tech. Paper* 3086.

ANDERSON, W. K. 1991*b* Numerical study on using sulfur hexafluoride as a wind tunnel test gas. *AIAA J.* **29**, 2179–2180.

BETHE, H. A. 1942 The theory of shock waves for an arbitrary equation of state. *Office of Scientific Research and Development*, Rep. 545.

BOBER, W. & CHOW, W. L. 1990 Nonideal isentropic gas flow through converging-diverging nozzles. *Trans. ASME* I: *J. Fluids Engng*, **112**, 455–460.

CRAMER, M. S. 1989*a* Negative nonlinearity in selected fluorocarbons. *Phys. Fluids* A **1**, 1894–1897.

CRAMER, M. S. 1989*b* Shock splitting in single-phase gases. *J. Fluid Mech.* **199**, 281–296.

CRAMER, M. S. 1991*a* Nonclassical dynamics of classical gases. *Nonlinear Waves in Real Fluids* (ed. A. Kluwick), pp. 91–145. Springer.

CRAMER, M. S. 1991*b* On the Mach number variation in steady flows of dense hydrocarbons. *Trans. ASME* I: *J. Fluids Engng* **113**, 675–680.

CRAMER, M. S. & BEST, L. M. 1991 Steady, isentropic flows of dense gases. *Phys. Fluids* A **3**, 219–226.

CRAMER, M. S., PARK, S. & WATSON, L. T. 1996 Suppression of shock-induced separation in dense gases. In *20th Int. Symp. on Shock Waves* (ed. B. Sturtevant, J. Shepherd & H. Hornung). World Scientific.

CRAMER, M. S. & TARKENTON, G. M. 1992 Transonic flows of Bethe–Zel'dovich–Thompson fluids. *J. Fluid Mech.* **240**, 197–228.

CRAMER, M. S., TARKENTON, L. M. & TARKENTON, G. M. 1992 Critical Mach number estimates for dense gases. *Phys. Fluids* A **4**, 1840–1847.

CRICKENBERGER, A. B. 1991 The dynamics of steady supersonic dense gas flows. Master's thesis, Virginia Polytechnic Institute and State University, Blacksburg, Virginia.

DZIEDZIC, W. M., JONES, S. C., GOULD, D. C. & PETLEY, D. H. 1993 Analytical comparison of convective heat transfer correlation in supercritical hydrogen. *J. Thermophys. Heat Transfer* **7**, 68–73.

ENKENHUS, K. R. & PARAZZOLI, C. 1970 Dense gas phenomena in a free-piston hypersonic wind tunnel. *AIAA J.* **8**, 60–65.

FLETCHER, C. A. J. 1988 *Computational Techniques for Fluid Dynamics*, vol. 2. Springer.

JONES, J. B. & HAWKINS, G. A. 1972 *Engineering Thermodynamics*. McGraw-Hill.

KLUWICK, A. 1991 Small-amplitude finite-rate waves in fluids having both positive and negative nonlinearity. In *Nonlinear Waves in Real Fluids* (ed. A. Kluwick), pp. 1–43. Springer.

KLUWICK, A. 1994 Interacting laminar boundary layers of dense gases. *Acta Mechanica* (Suppl) **4**, 335–349.

LAMBRAKIS, K. C. & THOMPSON, P. A. 1972 Existence of real fluids with a negative fundamental derivative Γ. *Phys. Fluids* **15**, 933–935.

LEIDNER, P. 1990 Realgaseinflüsse in der Gasdynamik. Diplomarbeit, Universität Karlsruhe, Karlsruhe, Germany.

LEUNG, J. C. & EPSTEIN, M. 1988 A generalized critical flow model for nonideal gases. *AIChE J.* **34**, 1568–1572.

MACCORMACK, R. W. 1969 The effect of viscosity in hypervelocity impact cratering. *AIAA Paper* 69–354.

MARTIN, J. J. & HOU, Y. C. 1955 Development of an equation of state for gases. *AIChE J.* **1**, 142–151.

MENIKOFF, R. & PLOHR, B. 1989 Riemann problem for fluid flow of real materials. *Rev. Mod. Phys.* **61**, 75–130.

MONACO, J. F. 1994 Supersonic flows of Bethe–Zel'dovich–Thompson fluids in cascade configurations. Master's thesis, Virginia Polytechnic Institute and State University, Blacksburg, Virginia.

MORREN, S. H. 1991 Transonic aerodynamics of dense gases. *NASA Tech. Mem.* 103722.

REID, R. C., PRAUSNITZ, J. M. & POLING, B. E. 1987 *The Properties of Gases and Liquids*, 4th edn. McGraw-Hill.

REYNOLDS, W. C. & PERKINS, H. C. 1977 *Engineering Thermodynamics*, 2nd edn. McGraw-Hill.

RIEDEL, L. 1954 Eine neue Universelle Damfdruckformel–Untersuchungten über eine Erweiterung des Theorems der übereinstimmenden Zustände Teil 1. *Chem. Ing. Tech.* **26**, 83.

SCHNERR, G. H. & LEIDNER, P. 1993 Numerical investigation of axial cascades for dense gases. In *Proc. Pacific Intal Conf. on Aerospace Science and Technology*, Tainan, Taiwan.

SIMEONIDES, G. 1987 The aerodynamic design of hypersonic contoured axisymmetric nozzles including real gas effects. *Von Karman Institute for Fluid Dynamics Tech. Mem.* 43. Von Karman Institute, Waterloo.

SIMEONIDES, G. 1990 The VKI hypersonic wind tunnels and associated measurement techniques. *Von Karman Institute for Fluid Dynamics Tech. Mem.* 46. Von Karman Institute, Waterloo.

TARKENTON, G. M. & CRAMER, M. S. 1993 Transonic flows of dense gases. *ASME Paper* 93-FE-9.

THOMPSON, P. A. 1971 A fundamental derivative in gas dynamics. *Phys. Fluids* **14**, 1843–1849.

THOMPSON, P. A. & LAMBRAKIS, K. C. 1973 Negative shock waves. *J. Fluid Mech.* **60**, 187–208.

WAGNER, B. & SCHMIDT, W. 1978 Theoretical investigation of real gas effects in cryogenic wind tunnels. *AIAA J.* **16**, 580–586.

ZEL'DOVICH, YA. B. 1946 On the possibility of rarefraction shock waves. *Zh. Eksp. Teor. Fiz.* **4**, 363–364.